Mechanics Research Communications 135 (2024) 104223

Contents lists available at ScienceDirect

Mechanics Research Communications

journal homepage: www.elsevier.com/locate/mechrescom

Fabric controls on fracture surface roughness of an architected rock material

Chaoyi Wang [a,*], Liyang Jiang [f], Antonio Bobet [c], Hongkyu Yoon [e], Laura J. Pyrak-Nolte [b,c,d]

[a] Atmospheric, Earth, & Energy Division, Lawrence Livermore National Laboratory, Livermore, CA 94550, USA
[b] Department of Physics and Astronomy, Purdue University, West Lafayette, IN 47907, USA
[c] Lyles School of Civil Engineering, Purdue University, West Lafayette, IN 47907, USA
[d] Department of Earth, Atmospheric, and Planetary Sciences, Purdue University, West Lafayette, IN 47907, USA
[e] Geomechanics Department, Sandia National Laboratories, Albuquerque, NM 87123, USA
[f] State Key Laboratory of Hydroscience and Engineering, Tsinghua University, Beijing, China

ARTICLE INFO

Keywords:
Rock fabric
Fracture roughness
Distinct element method
3D printed rock

ABSTRACT

Fluid flow through fractures is intimately linked to the fracture surfaces that define the void geometry through which fluids flow. Thus, an understanding of what controls fracture surface roughness is essential to the development of models for predicting fluid transport through fractured rock. The difficulty in predicting surface roughness arises from the complexity of rock which is inherently heterogeneous and nonuniform in composition, fabric, and structural components, even when samples are acquired from the same rock mass. Here, a benchmarked-simulation approach motivated from geo-architected 3D printed synthetic gypsum rocks is used to provide insight into the competing contributions from fabric and layering on fracture roughness formation. Simulation results from a discrete element model (Particle Flow Code, Itasca Consulting Group, Inc.) clearly indicate that the relative orientation between mineral layers and in-layer mineral fabric, and the variability in mineral bonding strengths determine whether anisotropic corrugated surfaces or isotropic surfaces are formed. Weak mineral layers oriented perpendicular to the applied load resulted in strong roughness anisotropy. Peak failure loads were found to vary up to 30% depending on the strength of the mineral fabric at the location of fracture initiation, which provides insight into the observed high variability in strength values of natural rock. The uniqueness of induced fracture roughness and peak failure load is intimately linked to layering, mineral fabric, and their distribution in the rock. These findings have important implications for any architected material fabricated through serial printing of layers with local compositional heterogeneity.

1. Introduction

Layered rock often exhibits anisotropic material properties as well as strong spatial variability in response to applied loads because of the heterogeneous distributions of minerals within and among the layers. When layered rock is subjected to large stresses from fluid pressure, thermal stress, or other external perturbations, damage often results in the form of micro-fractures. Micro-fractures can coalesce into a process zone, which can eventually lead to macroscale fractures [1]. Natural fractures in layered rocks may have corrugated surfaces (Fig. 1(a–c)), which enables unobstructed fluid flow in the direction parallel to the corrugation ridges [2] (Fig. 1d). Understanding the material properties and the physical-chemical mechanisms that give rise to corrugated fracture surfaces in layered rocks can significantly benefit unconventional oil and gas recovery, geothermal stimulation, and carbon storage, through the prediction of fracture geometry to aid the optimization of energy production from the Earth's subsurface.

Previous studies suggest that fracture roughness and multi-scale mechanical properties are affected by grain size, failure mode, stress history, mineralogy, rock fabric, stress orientations, and geochemical interactions that can alter bond strengths of constituents [3–8]. More recent studies found that fracture toughness and roughness are strongly influenced by the layer and mineral fabric orientations in the rock [9,10] because both introduce mechanical anisotropy to the rock. Layering (lamination or bedding planes) is usually viewed as potential "planes of weakness" because it features low tensile and shear resistance to failure, leading to preferential failure paths along which fractures propagate, even when the initial fracture growth is perpendicular to the bedding

* Corresponding author.
E-mail address: wang140@llnl.gov (C. Wang).

https://doi.org/10.1016/j.mechrescom.2023.104223
Received 1 January 2023; Received in revised form 23 October 2023; Accepted 29 November 2023
Available online 30 November 2023

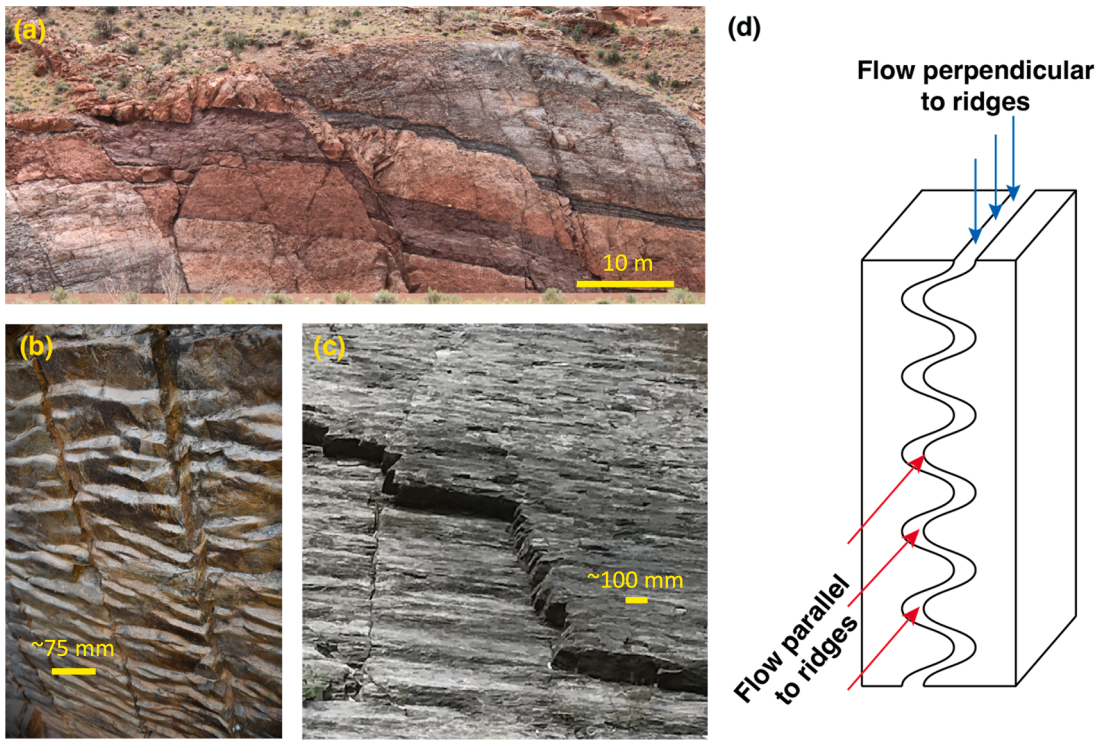

Fig. 1. (a) Moab fault, near the entrance to Arches national park (courtesy of Yoon), Utah. (b) & (c) sedimentary rock, Lederderg State Park, Australia (2019 courtesy of Pyrak-Nolte). (d) Fractures with strong roughness anisotropy (corrugation) can lead to strong anisotropy in hydraulic conductivity because fluid flow parallel to the corrugation ridges is relatively unobstructed compared to flow in the perpendicular direction.

planes [11]. Mineral fabrics in rocks introduce mechanical anisotropy through the interplay of strain history, localized strength distribution, and preferred mineral orientation [12–16]. Mechanical anisotropy can cause fracture propagation to deviate from a straight path. Although rock layering and mineral fabrics are clearly linked to fracture toughness and roughness, predicting the fracturing behavior of natural rocks remains difficult because of their inherent heterogeneity [8,17]. Laboratory tests using natural rock samples often vary significantly in test results. For example, the fracture toughness of natural shale specimens may exhibit a range of variability due to local heterogeneity for the same relative layering orientation with respect to the direction of loading [18].

A recent study [19] created "geo-architected" rock specimens through additive manufacturing (i.e., 3D printing) which enabled control over layer and mineral fabric orientation. The "geo-architected" rocks were printed by bonding bassanite (calcium sulfate hemi-hydrate, $2CaSO_4{\cdot}H_2O$) layers with a proprietary water-based binder agent that produced gypsum ($CaSO_4{\cdot}2H_2O$) as a reaction product (gypsum-bassanite bonds). The spreading pattern of the binder agent formed in-layer mineral fabrics (gypsum-gypsum bonds). The orientation of the mineral fabric was determined by the direction of movement of the spray nozzle (Fig. 2a). The gypsum formed stronger bonds between gypsum crystals than with bassanite, resulting in the anisotropy in mechanical properties. Optical images of thin sections from the samples display the mineral fabric (Fig. 2c) and layering (Fig. 2d and e) and both resulted from the 3D printing process. Results from three-point bending (3 PB) tests on center-notched 3D printed rocks showed that the in-layer fabric orientation affected the fracture toughness and fracture roughness of the specimens [19]. Reconstruction of the fracture surfaces from X-ray tomographic reconstructions indicated that the fracture path deviated from the vertical plane (Fig. 2b), forming corrugations (Fig. 2b) in some instances. The study [19] found that the fracture trace geometry was affected by layering and in-layer fabric orientation. Both factors contributed to the resistance to cracking and caused the propagating fracture to deviate. However, it is challenging to study the individual effects of the structural and fabric components on the fracturing mechanisms in the laboratory tests. Three-point bending (3 PB) test results on specimens with similar structural arrangement showed noticeable differences in fracture roughness and peak loads (around ~10% compared to ~25% in natural rocks [20]). While this variation can normally be explained by natural heterogeneity in natural rocks, it cannot be easily justified using 3D printed samples. In addition, the experiments showed that strongly corrugated surfaces occurred when the geometric toughening from the layers and fabric acted in the same direction; isotropic fracture surface roughness (non-corrugated) was obtained when the fracture failure path was perpendicular to both the layering and the fabric (i.e., the resistance to failure from the fabric and layers acted in orthogonal directions). The objective of this paper is to quantitatively investigate the impact of fabric and layering on the fracture toughness of the 3D printed gypsum, and their impact on the roughness of the fracture produced during 3 PB tests. We achieve this by performing computational simulations using a discrete element model.

2. Numerical model

We built a digital rock model using a discrete element method (DEM) [22] to quantify how layer orientation, in-layer mineral fabric, and variability of mineral bonding strength affect fracture roughness and peak loads in three-point bending (3 PB) loading tests. The rock is simulated as an ensemble of particles that are bonded. The constitutive model for the particle interaction mimics the cementation of granular materials [23]. Fracture propagation is represented by bond breakages (micro-cracks) that can coalesce into a macroscale fracture and can propagate through inter-particle contacts. Spatially distributed physical properties can be assigned to particles and contact bonds to simulate layering and mineral fabric, separately. We used the commercially available software package, Particle Flow Code 3D (PFC 3D, Itasca Consulting Group, Inc.) to reproduce the geometry and mechanical

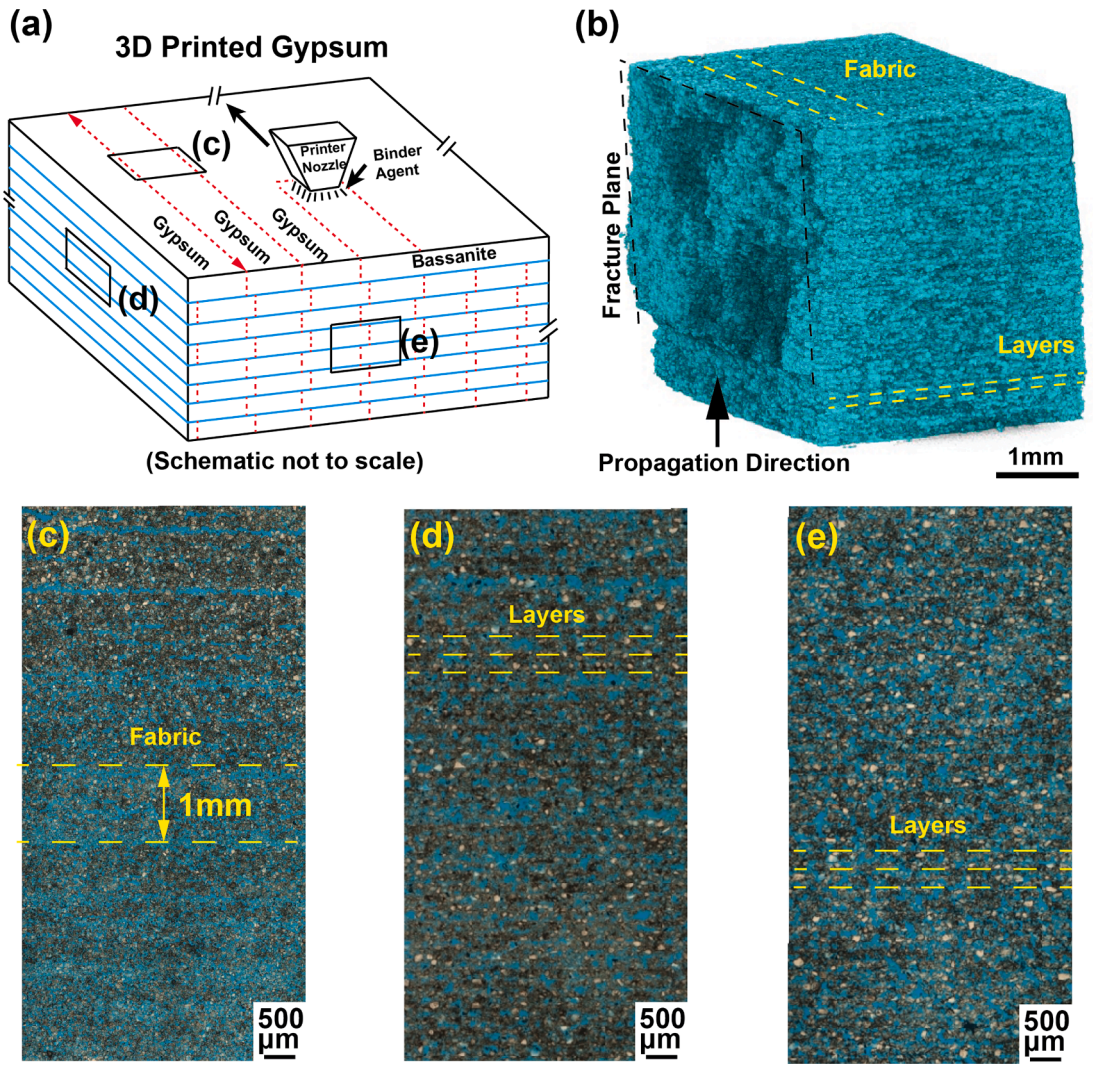

Fig. 2. (a) Schematics of the 3D-printing process. Layers are formed by depositing bassanite powder (blue lines), and mineral fabric is created from the spreading of the bonding agent from the printer nozzle (red dashed lines). (b) An X-ray CT image of 3D printed rock after three-point bending test shows fracture propagation from the notch (picture courtesy of Jiang). (c), (d), (e) Thin section images of the 3D printed rock showing layering and mineral fabric. Thin section images are available from the dataset of Damage Mechanics Challenge [21].

behavior of the geo-architected rock used in three-point bending tests (3 PB) [19].

The digital rock model consists of mechanically bonded particles of a uniform size (423 μm in diameter). The model is 7.62 cm in length, 2.54 cm in height, and 1.27 cm in thickness (180 × 60 × 30 particles, respectively), representing the external dimensions of the laboratory samples [19]. The size of the particles in the numerical model is chosen to approximate the behavior of the samples in the laboratory, while balancing computational cost. There is a center notch (0.13 cm by 0.51 cm) on each sample. The different simulated geometries are labeled using the conventional classification of layered specimens (arrester, divider, and short traverse [19]) that is based on the orientation of the layers relative to the fracture propagation plane (Fig. 3a). Each geometry has two variants because the orientation of the in-layer mineral fabric depends on the direction of the printer head movement during printing. The variants are referred to as: H and Halt for arrester, VV and VValt for divider, V and Valt for short traverse (Fig. 3b). Fig. 3c shows a schematic of the 3 PB tests used to create tensile fractures in the 3D-printed rock samples.

In the simulations, several assumptions are made: (1) the bassanite-gypsum interfaces between layers are planes of weakness that have lower bonding strength than the gypsum matrix (layers); (2) in-layer fabric is represented by periodic particle bands whose bonding strengths are spatially varied and are offset between layers, as previously observed in the thin section images from the specimens (Fig. 2); (3) inherent material heterogeneity is represented by a random variability of bonding strength of up to 60%. Fig. 4a shows the layers and in-layer mineral fabric. Each layer is 1.3 mm thick. Each fabric band (top-left zoom of Fig. 4a) is approximately 4.2 mm in width and 1.3 mm in height and has a spatial distribution of bonding strengths that follow a parabolic decay with a maximum strength at the center that decreases to 40% of the maximum strength at the edges. The purpose of this arrangement of layers/fabrics is to represent the same structure formed by the deposition of the bassanite powder and the spraying of the chemical binder from the printer head (nozzle) during 3D printing, as the edges of the band receives less binding agent than the center [24]. A 30 % inter-layer offset is used for the fabric. Variability of bonding strength is applied to the model following a uniform distribution (Fig. 4b) to simulate heterogeneity in the material. The model parameters are listed in Table 1. The parameters are calibrated using laboratory test results [19]. All simulations have been performed at a constant quasi-static loading rate of 0.5 μm/s, identical to that applied in the laboratory [19]. In the simulations, the loading ceased once the force on the loading pin dropped below 10% of the peak load. The two halves of

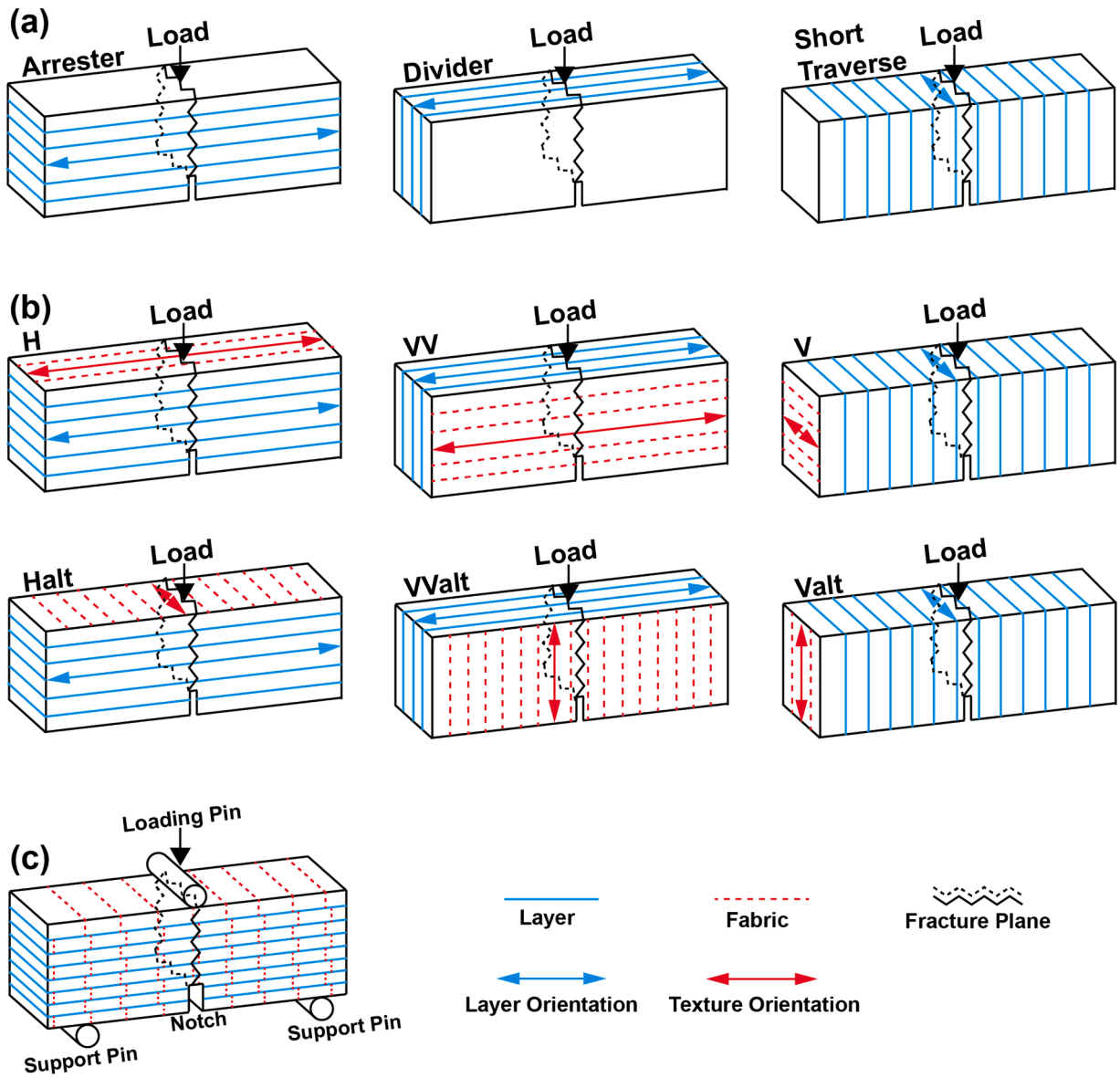

Fig. 3. (a) Sample naming conventions regarding the relative orientation of the layers to the fracture propagation plane, i.e., arrester, divider, and short traverse. (b) Orientation of layering and fabric with respect to the fracture propagation plane: arrester (H, Halt), divider (VV, VValt), and short traverse (V, Valt). (c) A schematic for laboratory samples (e.g. Halt) subjected to three-point-bending tests. The layers and mineral fabric in the schematics are not drawn-to-scale.

the failed sample are numerically separated to expose the fracture surface and then are straightened to remove any rigid body rotations induced by the failure of the specimen. The roughness of the fracture is obtained by measuring the distance between the actual fracture surface and a reference plane, i.e., a vertical plane (x-y plane in Fig 4a) through the center of the notch.

3. Influence of layer, in-layer fabric, and bonding strength variability

Before testing the combined influence of three factors (i.e., layer, in-layer fabric, and variability in bonding strength), we performed a systematic study for arrester geometry (H and Halt) using a single or the combination of the three factors (Table 2) to identify the contribution from each factor and/or multiple factors to fracture surface roughness.

The fracture roughness profiles for arrester samples H and Halt are shown in Figs. 5 and 6, respectively. First, Figs. 5a and 6a show the orientation of the layers and fabric for the sample H and Halt. Figs. 5b–h and 6b–h contain the fracture surface roughness profiles above contour maps of the asperity heights, for all the simulations listed in Table 2, except H-2 and Halt-2. No fracture roughness is observed when none of the factors are included in the simulations. For example, H-1 and Halt-1 represent homogeneous isotropic specimens that formed smooth surfaces under the 3 PB conditions (Figs. 5b and 6b). Sample H-2 and Halt-2 contained only layers, which resulted in excessive fracture propagation along the layer boundaries causing no vertical fractures to propagate. H-3 and Halt-3, with only in-layer fabric, produced anisotropic surface roughness with very small amplitude corrugations for H3 (Fig. 5c). Roughness anisotropy is observed in Halt-3 (Fig. 6c) but with corrugations on the order of the sample size. H-4 and Halt-4 were constructed with only a random variability in inter-particle bonding strength, producing an isotropic surface roughness (Figs. 5d and 6d). H-5 and Halt-5 have both layers and in-layer fabric. This combination of factors resulted in fractures with significant anisotropy along the x direction with large amplitude corrugations (Figs. 5e and 6e). When both in-layer fabric and bonding strength variability are included (H-6 and Halt_6), moderate amplitude roughness is observed with no significant anisotropy (Figs. 5f and 6f). H-7 and Halt-7 simulations had both layer and bonding strength

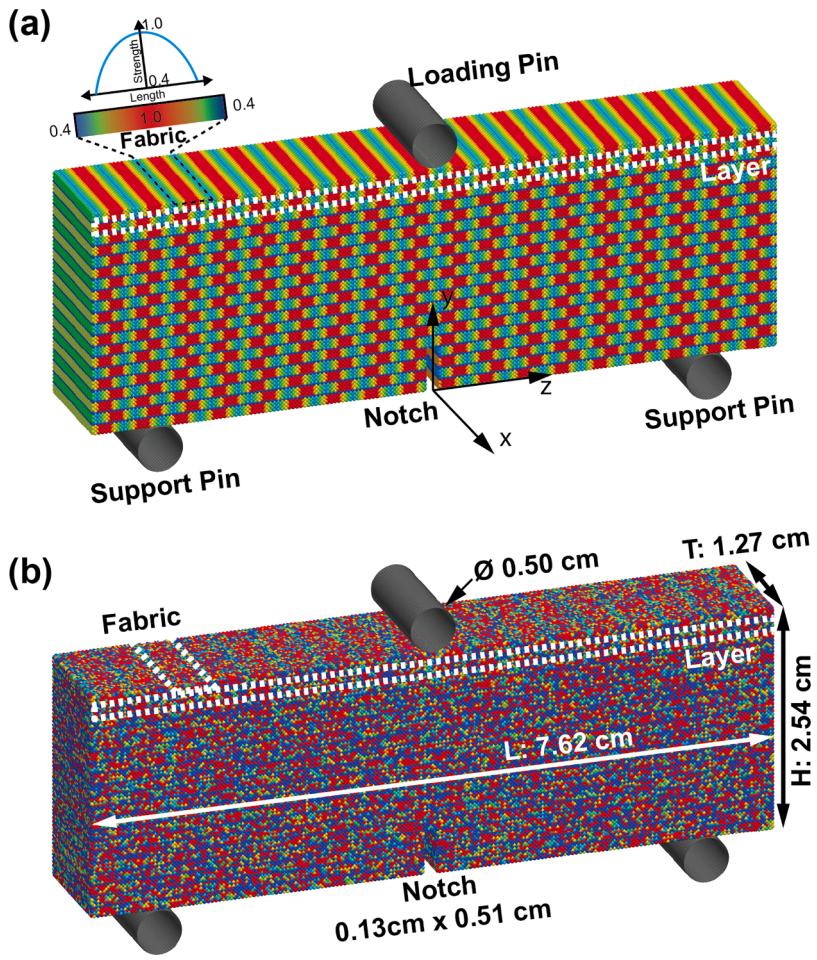

Fig. 4. (a) Illustration of the layering and fabric for Halt sample; the fabric strength distribution is a parabolic decay from maximum (100%) strength at the center to 40% at the sides; the in-layer fabric has an offset of 30% of its width between layers. (b) Final model for Halt sample that includes a variability in bonding strength.

Table 1
Model parameters.

Parameter	Value	Unit
Particle Diameter	423	μm
Density[a]	2650	$\times 10^8 kg/m^3$
Effective Modulus	850	MPa
N-to-S Ratio[b]	1.0	
Inter-Particle Friction	0.3	
Bond Effective Modulus	850	MPa
Bond N-to-S Ratio	1.0	
Bond Tensile Strength	15	MPa
Bond Cohesion	12.5	MPa
Bond Friction Angle	45	Degree
Layer Strength Ratio	0.3	
Fabric Strength Ratio	0.4–1.0	
Inter-Layer Offset	0–30%	
Randomness	60%	

[a] Density is scaled to speed up simulation, the average time step in the simulation is 10^{-4} s.

[b] Effective modulus (E^*) and Normal-to-Shear (N-to-S) ratio (κ^*) are used to calculate normal and shear stiffness at the particle contact. $k_n = \frac{E^*}{L}$, $k_s = \frac{k_n}{\kappa^*}$, k_n and k_s are normal and shear stiffness at the contact, respectively, L is the distance between the centroids of two contacting particles.

Table 2
Cases examined for the numerical analysis.

Sub-Configurations	Layer	In-layer Fabric	Randomness
H-1/Halt-1	×	×	×
H-2/Halt-2	√	×	×
H-3/Halt-3	×	√	×
H-4/Halt-4	×	×	√
H-5/Halt-5	√	√	×
H-6/Halt-6	×	√	√
H-7/Halt-7	√	×	√
H-8/Halt-8	√	√	√

variability. These simulations produce roughness with very strong corrugations. H-8 and Halt-8 included all three factors in the simulations. H-8 (Fig. 5h) exhibits an isotropic fracture roughness while Halt-8 (Fig. 6h) has an anisotropic roughness with corrugations following the orientation of the fabric. The simulation results of surface roughness in H-8 and Halt-8 agree with those observed in the laboratory data [19].

From the simulation results, the following observations are made: (1) layerscontribute strongly to roughness anisotropy if oriented perpendicular to loading direction (H-5/Halt-5, H-7/Halt-7), producing corrugation amplitudes much larger than in the laboratory experiments [19]; (2) variability in bonding strength contributes to isotropic roughness (H-4/Halt-4), but it alone cannot produce anisotropic fracture roughness; (3) the in-layer fabric orientation constrains the excessive corrugation amplitude caused by layers. This is evident in a comparison of H-7/Halt-7 (without fabric) with H-8/Halt-8 (with fabric) where the

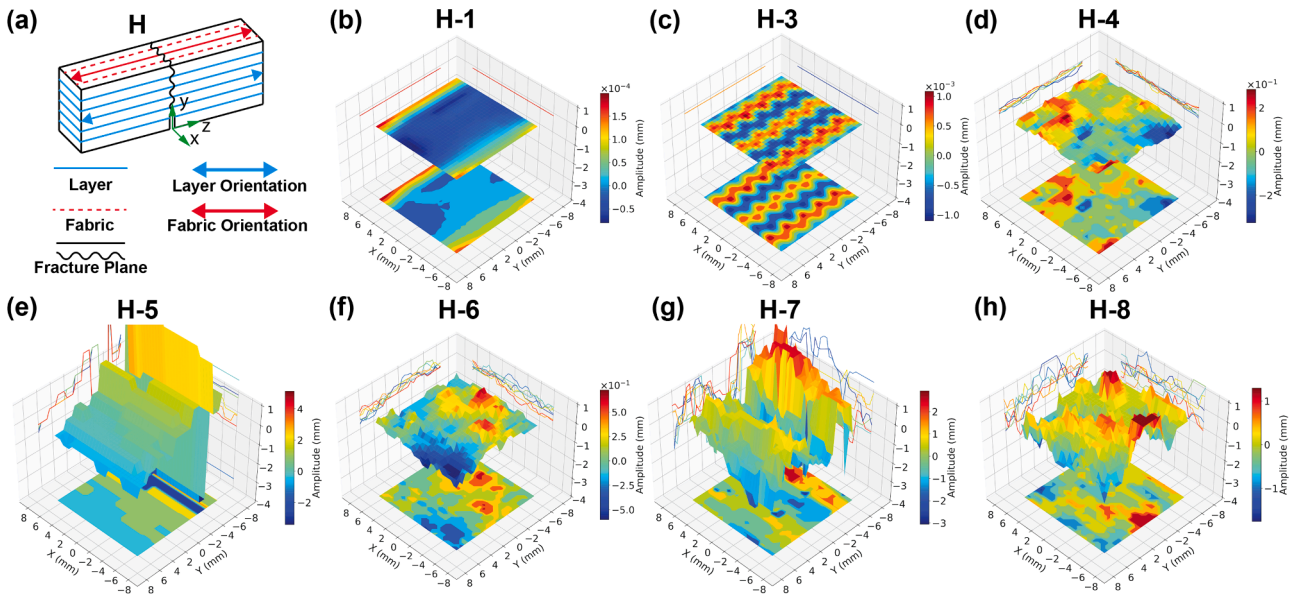

Fig. 5. 3D roughness profiles for the tensile fractures induced in H sub-configurations, the 2D projected contour plots on the bottom show asperity heights. H-2 failed to produce a vertical fracture; therefore, no fracture profile is shown for H-2. (Assumed configurations are listed in Table 2).

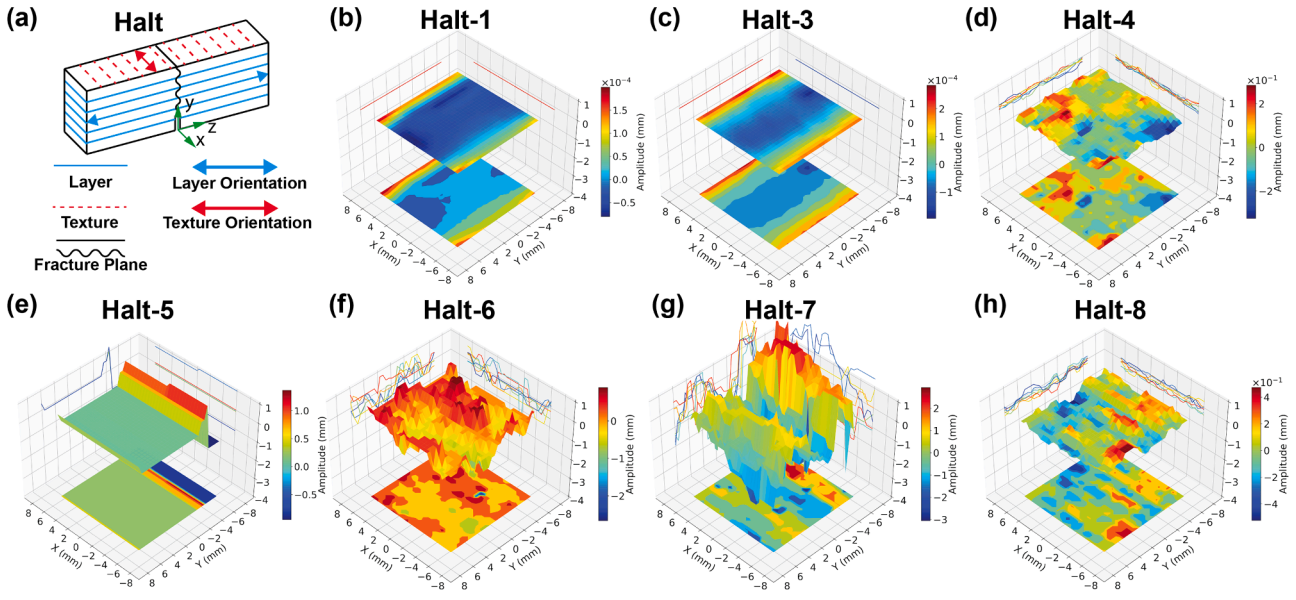

Fig. 6. 3D roughness profiles for tensile fractures induced in Halt sub-configurations, the 2D projected contour plots on the bottom show asperity heights. Halt-2 failed to produce a vertical fracture; therefore, no fracture profile is shown for Halt-2. (Assumed configurations are listed in Table 2).

constraint is weaker when the in-layer fabric is oriented parallel to the fracture plane (Halt-8, anisotropic roughness) than when it is perpendicular (case H-8 isotropic roughness). In summary, all three factors including layer, in-layer fabric, and random variability of bonding strength are required (H-8/Halt-8) to reproduce the fracture roughness profiles for H and Halt samples observed in the laboratory [19].

We perform additional simulations for arrester (H/Halt), divider (VV/VValt), and short traverse (V/Valt) geometries that included all three factors. The simulation results are shown in Fig. 7. An isotropic surface roughness is observed for case H (Fig. 7a) and case VV (Fig. 7c) because the orientations of the layers and the in-layer mineral fabric are both perpendicular to the fracture plane. Cases Halt (Fig. 7b) and VValt (Fig. 7d) show corrugations with a significant roughness anisotropy. The ridges of the corrugations are parallel to the direction of in-layer fabric, i.e., Halt in the x-direction and VValt in the y-direction. As explained before, inside each fabric band, the bonding strength on the two edges are weaker (Fig. 4a), thus providing an alternative propagation path across layers for the fracture growth. When layers and in-layer fabric are both parallel to the fracture plane (V, Fig. 7e and Valt, Fig. 7f), smooth fracture surfaces are formed because the fracture tends to propagate along the weak layer boundaries. The in-layer mineral fabric in V and Valt samples creates corrugation with small amplitudes parallel to the fabric orientation, i.e., in the V sample, along the x-direction and in the Valt, along the y-direction. The simulation results are consistent with those in the laboratory experiments [19].

The fracture roughness in the simulations is further examined using 2D auto-correlation analysis. Details of the method are given in [19]. Roughness anisotropy exists when the shape of the contours is elliptical. If the contours are circular or nearly circular, the roughness is taken to be isotropic. Contours of the normalized auto-correlation functions from

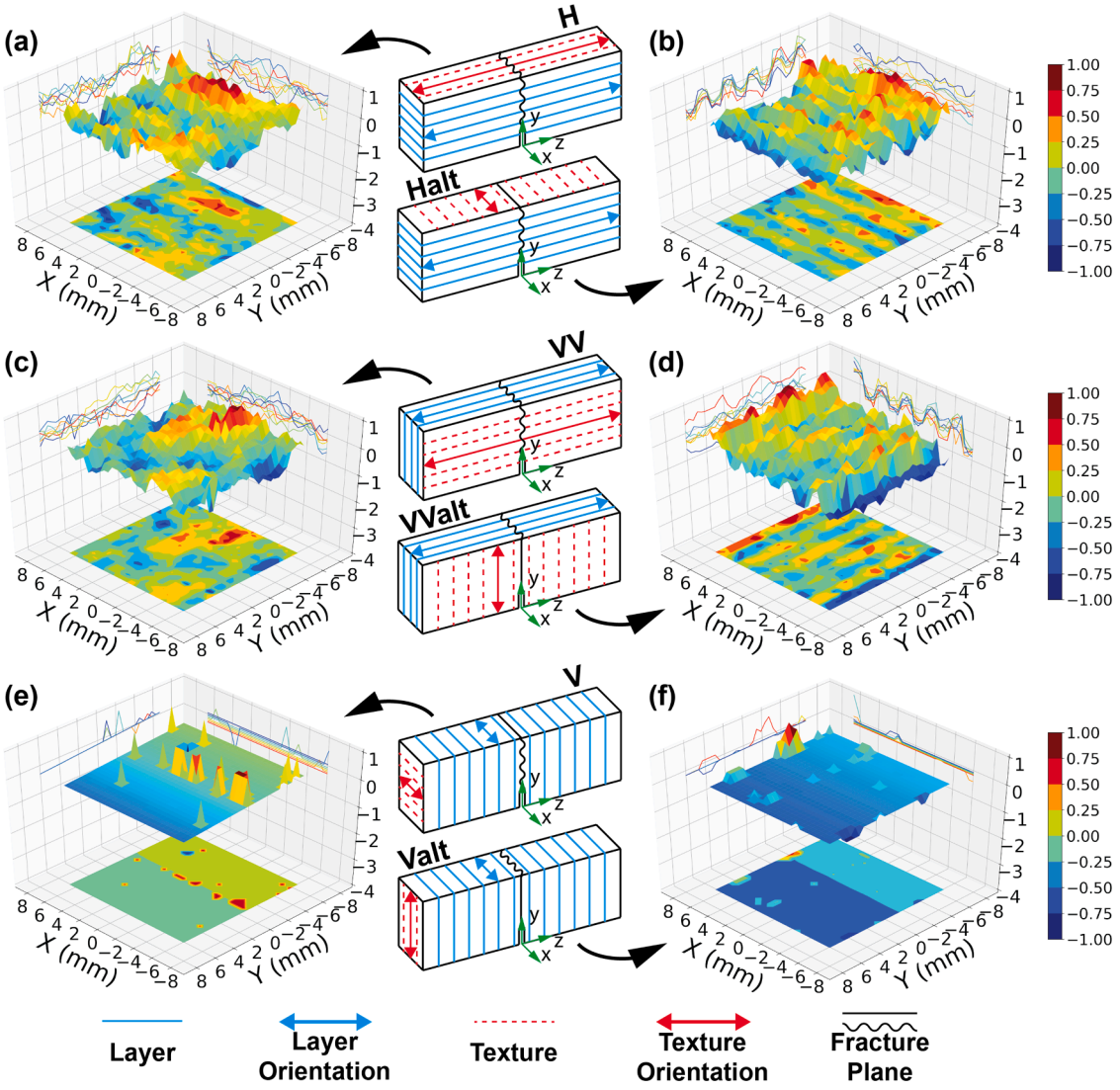

Fig. 7. 3D roughness profiles of the tensile fractures induced in the digital rock samples: (a) H, (b) Halt, (c) VV, (d) VValt, (e) V, (f) Valt. Each roughness profile is the average of four simulations with different random seeds. The amplitude of the roughness is normalized by the largest absolute asperity height in each profile.

both simulations and laboratory measurements [19] are presented in Fig. 8. For H and VV samples, the layer and fabric orientations are both perpendicular to the fracture plane. This creates roughness in both the x- and y-directions, which results in nearly isotropic roughness (i.e., nearly circular contours in Fig. 8a–d). For Halt and VValt samples, where the layers are perpendicular to the fracture plane and the mineral fabric is parallel to the fracture plane, the fracture roughness is strongly anisotropic (Fig. 8e–h), producing contours that are highly elongated, with the elongation parallel to the corrugation ridges. Roughness anisotropy is also produced when the layer and fabric are both parallel to the fracture plane (Fig. 8i–l). The elongation direction of the contours occurs along the corrugation ridges. The anisotropy produced in the numerical simulations for V and Valt samples (Fig. 8i and k) is not as strong as that observed in the laboratory (Fig. 8j and l).

Previous studies have shown that Mode I fracture toughness, K_I, is affected by layer orientation [18,19]. In shales, it has been observed that the divider geometry has the highest fracture toughness followed by the arrester and then by the short traverse (Fig. 3) [9,10,18]. The peak load (i.e., the load at failure) of the 3 PB tests can be taken as a measure of fracture toughness (note that because the notch in the 3D printed samples is not sharp, the load at failure may not be directly related to fracture toughness). Fig. 9 compares the peak loads obtained from the simulations with those from the laboratory experiments [19]. The peak loads are normalized by the peak load of sample H, which is the largest. The error bars in the figure describe the different results obtained from the numerical simulations (four simulated 3 PB tests were conducted on each sample configuration with different initial seeds to generate the random distribution of inter-particle bonding strength; this is discussed later) and from the experiments (using samples from different printing cohorts). The simulation results are consistent with those from the laboratory in terms of the order of the peak loads, i.e., H and VV samples have the largest 3 PB peak loads, followed by Halt and VValt samples; V and Valt samples have the smallest 3 PB peak loads.

4. Discussion

4.1. Effects of in-layer fabric arrangement

As mentioned previously, the roughness of a fracture determines its hydraulic conductivity, as well as its mechanical response [15,17,25]. It is crucial to understand what controls the roughness of a fracture when it is formed. Further, it is possible to relate variability of measurements in architected rock materials to micro-scale characteristics of the in-layer fabric.

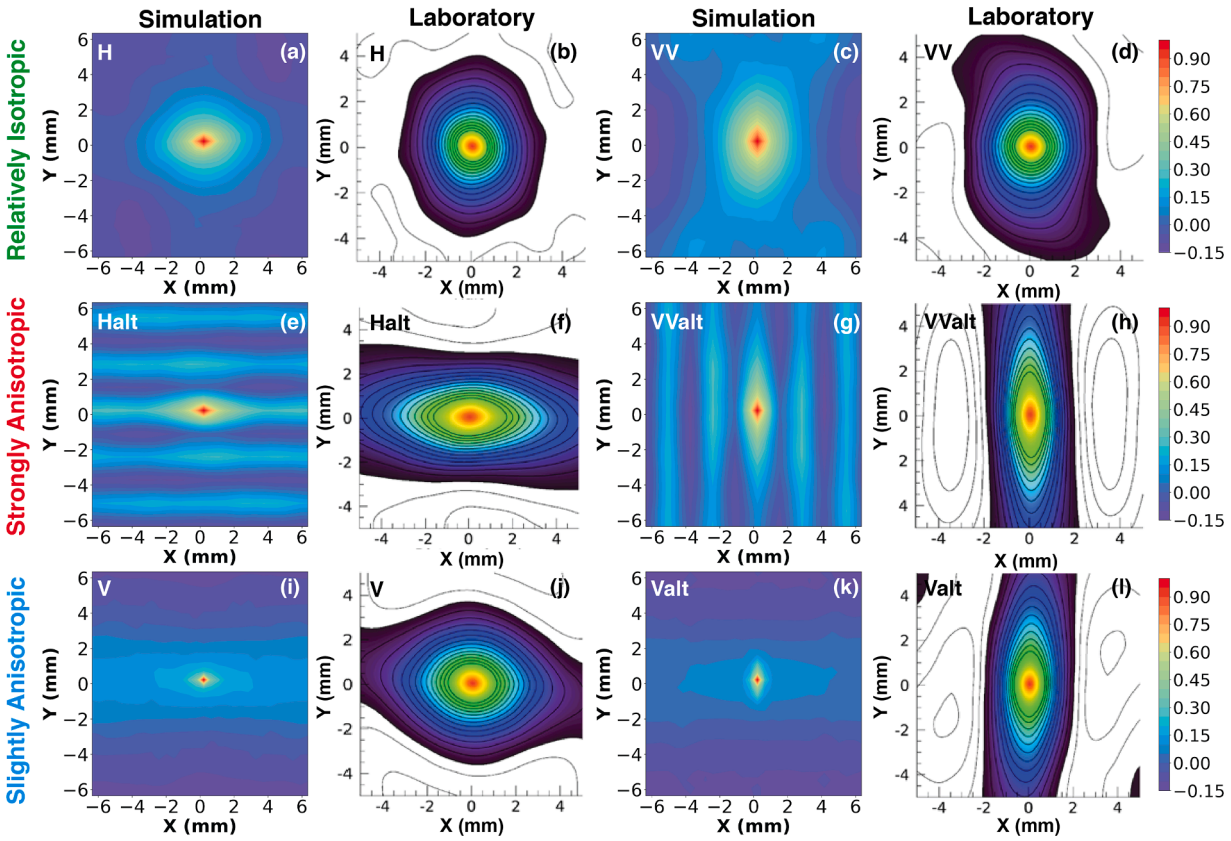

Fig. 8. Comparison of normalized 2D auto-correlation functions between simulations and laboratory measurements for: (a), (b) sample H; (c), (d) sample VV; I, (f) sample Halt; (g), (h), sample VValt; (i), (j) sample V; and (k), (l) sample Valt.

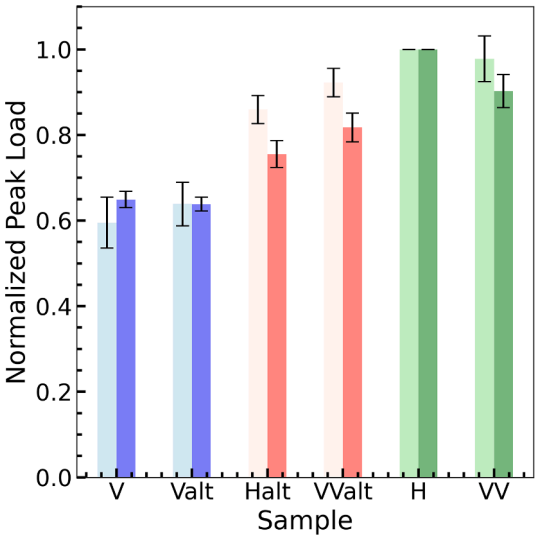

Fig. 9. Comparison of normalized peak loads obtained from simulations and from laboratory experiments (normalized with respect to H peak load). Laboratory results are shown by the lighter color (left bar) than the simulations (right bar).

Laboratory tests on natural rock show high variability in measured mechanical strengths, of about 30% to 50% between different tests [8–10,18]. Fig. 9 shows the comparison of peak load values for all six sample configurations, with the error bars resulting from four different simulations with different random seeds for bonding strength variability. This induces a small variability in the peak load for each sample, which is much lower than that of natural rocks. We hypothesize that the large variability exhibited in natural rock materials is attributed to weak areas near the crack initiation location. To validate this hypothesis, additional simulations were performed using the Halt sample design but with offset fabric bands, with increments in offset of 20% of the total band length: from 0% (perfect alignment) to 100% (perfect alignment recovered) from layer to layer (see Fig. 10a). All other parameters are held constant. The offset changes the local distribution of bonding strengths above the notch (Fig. 10a). Fig. 10b shows that the peak loads of samples with 0% to 40% offset are higher by ~ 30% than for offsets of 60% or greater. This is attributed to the high bonding strength in the notch tip areas where the fracture must initiate (Fig. 10a, 0%, 20%, 40% offset). Conversely, the peak loads are lower when the notch tip falls within a zone with weak strength (Fig. 10a, 60%, 80%, 100% offset). Thus, the location of the notch with respect to the mineral fabric affects the material strength by as much as 30%, which is comparable to the variability observed in natural rock.

The auto-correlation analysis of the fracture roughness profiles from the offset fabric band simulations is shown in Fig. 10c–h. Samples with 0% and 100% of in-layer fabric offsets have nearly isotropic fracture surface roughness (Fig. 10c and h). Roughness anisotropy increases with increasing fabric offset up to 60%, as seen in Fig. 10d–g, where the contours are stretched along the x-direction. Both mineral fabric and fabric offsets from layer to layer are necessary conditions for developing roughness anisotropy or corrugations in tensile fractures.

In nature, however, mineral fabric may display much greater complexity [8] (e.g., variability in strengths and length scales of cemented and grain materials, compositional heterogeneity, and existing pores, etc.). Certainly, more research is needed to better understand the consequences of such complexity. However, the findings from the simulations point towards a more prominent influence of mineral fabric on rock strength and fracture roughness than previously envisioned.

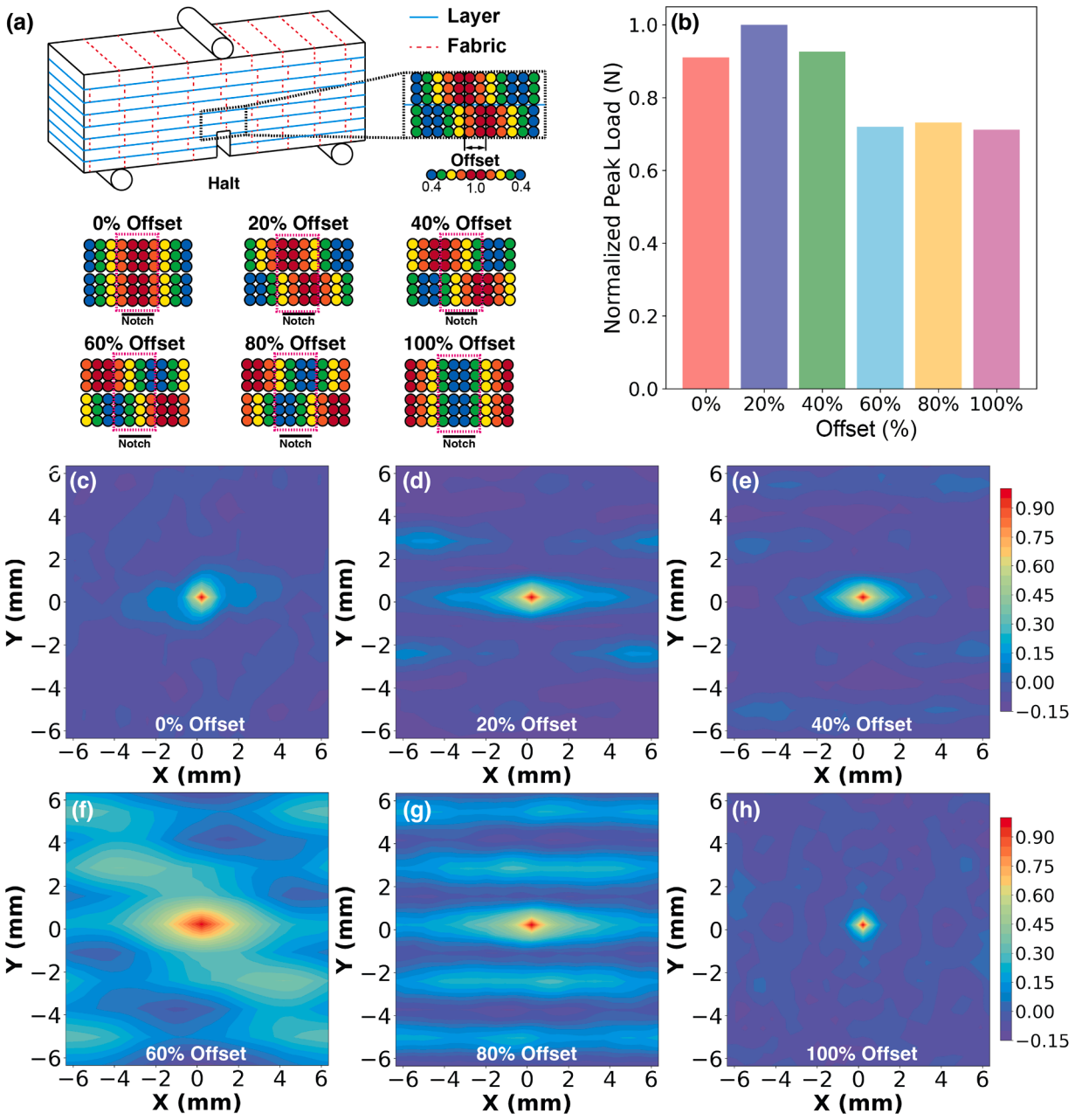

Fig. 10. (a) Schematic of the inter-layer offsets of fabric bands in Halt samples; each circle represents a particle in the model, and the colors indicate its relative bond strength (100% by red color to 40% by blue color). (b) Peak loads obtained from simulations of 3 PB tests on Halt samples. (c) to (h) Auto-correlation functions of fracture roughness for the same samples.

4.2. Effects of bonding strength variability

Fig. 11 shows the simulation results from Halt and VValt samples with and without bonding strength variability. The fracture roughness profiles, obtained from the simulations without the random bonding strength variability (Fig. 11a and c), are anisotropic with non-repeating corrugations followed by a flat surface, which are different from laboratory results [19]. Fracture roughness profiles from samples with bonding strength variability exhibit corrugations (Fig. 11b and d), which match the laboratory results closely. This observation suggests that bonding strength variability is necessary to capture the fracture roughness of the architected rock material.

4.3. Effects of particle size

The influence of grain size on the simulation results was explored by reducing the grain diameter by half, from 423 μm to 212 μm. As a result, the fine-scale digital rock model consists of 360 × 120 × 60 particles. The smaller grain size slightly improves the resolution of the roughness profiles but at the cost of increasing computational time by a factor of 20, which makes the simulations too expensive. The simulations with the larger number of grains show no significant difference in terms of roughness anisotropy (Fig. 12c, e, g, k, i and m). It is worth noting that with the larger number of particles, the peak failure loads for V and Valt samples (both short traverse) are slightly higher than those from the original simulations (Fig. 12a, right columns). A possible reason for this is that the mechanical parameters used for the contacts need to be re-calibrated.

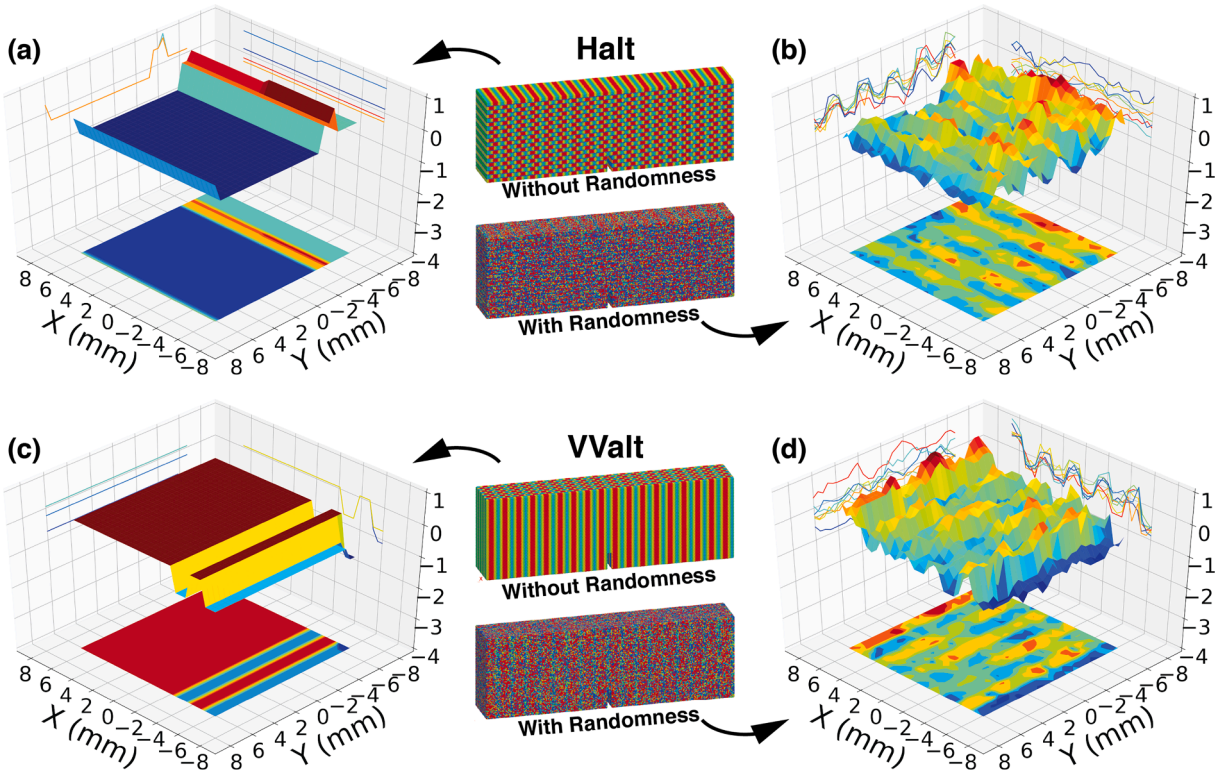

Fig. 11. Comparison between models with and without bonding strength variability. (a) and (b) show the fracture roughness of the Halt sample with and without bonding strength variability. (c) and (d) are analogous plots but for the VValt sample.

4.4. Model scalability

The scalability of the model is explored by increasing/decreasing the inter-particle bonding strength by a factor of two. Only one simulation has been conducted for each sample geometry with the new bonding strengths. The peak loads obtained are summarized in Fig. 12a (left columns). There is no significant difference between the scaled and the base simulations in terms of peak load ranking order (H, VV $>$ Halt, VValt $>$ V, Valt). The roughness anisotropy characteristics (not shown) are also similar. These simulation results suggest that fracture roughness anisotropy is not controlled by the absolute magnitude of the bond strength, but rather by the structural components, namely: layers, in-layer fabric and variability of bonding strength.

5. Conclusions

This study shows the importance of layering and fabric on the tensile strength and fracture roughness of architected materials and explains the variability of laboratory test results that traditionally has been attributed to material heterogeneity. The results and findings from this study provide insight into fracture formation, peak loading, and fracture roughness, which is important to any application that builds a structure through serial printing of material layers that are bonded through chemical and/or thermal processes. The physical and chemical processes of 3D printing result in an inherent anisotropy in material properties and in how the material fails. 3D printing is now being developed for various engineering purposes with applications in automotive, aerospace, medical, and food industries [26–28]. In civil engineering, 3D printing is used for manufacturing of affordable housing and irregular shaped structures, repairing historical structures, and building extraterrestrial human colonies on the moon and other planets [29–34], etc. The design and fabrication of robust, safe, and sustainable infrastructure with 3D printing requires insight into how layered material fails and how the printing process can lead to an in-layer fabric that affects failure, the resultant fracture geometry, and variability in peak failure load.

Here, we created a digital rock model to include, explicitly, layering, in-layer fabric, and bonding strength variability, to simulate the fracture surface roughness and peak loads of 3 PB tests conducted on an architected rock material. A number of simulations with the DEM code PFC were completed to investigate the factors that control fracture surface roughness anisotropy, as observed in the laboratory experiments [19]. We use these simulations to explore the cause of the variability in peak load often observed in natural rock and in architected rock, but to a lesser extent. Comparison of numerical and laboratory results shows that strong roughness anisotropy emerges in tensile fractures when the layers and in-layer mineral fabric provide resistance to failure in the same direction. Fracture roughness anisotropy is suppressed if the layering and mineral fabric provide orthogonal resistance to failure. Results from the numerical simulations also show that variability of bonding strength is required to produce fracture surface roughness. Additionally, weak/strong areas around the fracture initiation location can greatly affect the peak failure load in 3 PB tests, by as much as 30%. The digital rock model seems relatively robust in terms of scaling. There are limitations including using a relatively large and uniform particle size and high computational cost when running high-resolution simulations with small particle sizes. Understanding how layered rock fails and forms the geometry through which fluid flows is essential for the optimization and sustainability of unconventional resources recovery, enhanced geothermal stimulation, and geologic carbon and hydrogen storage.

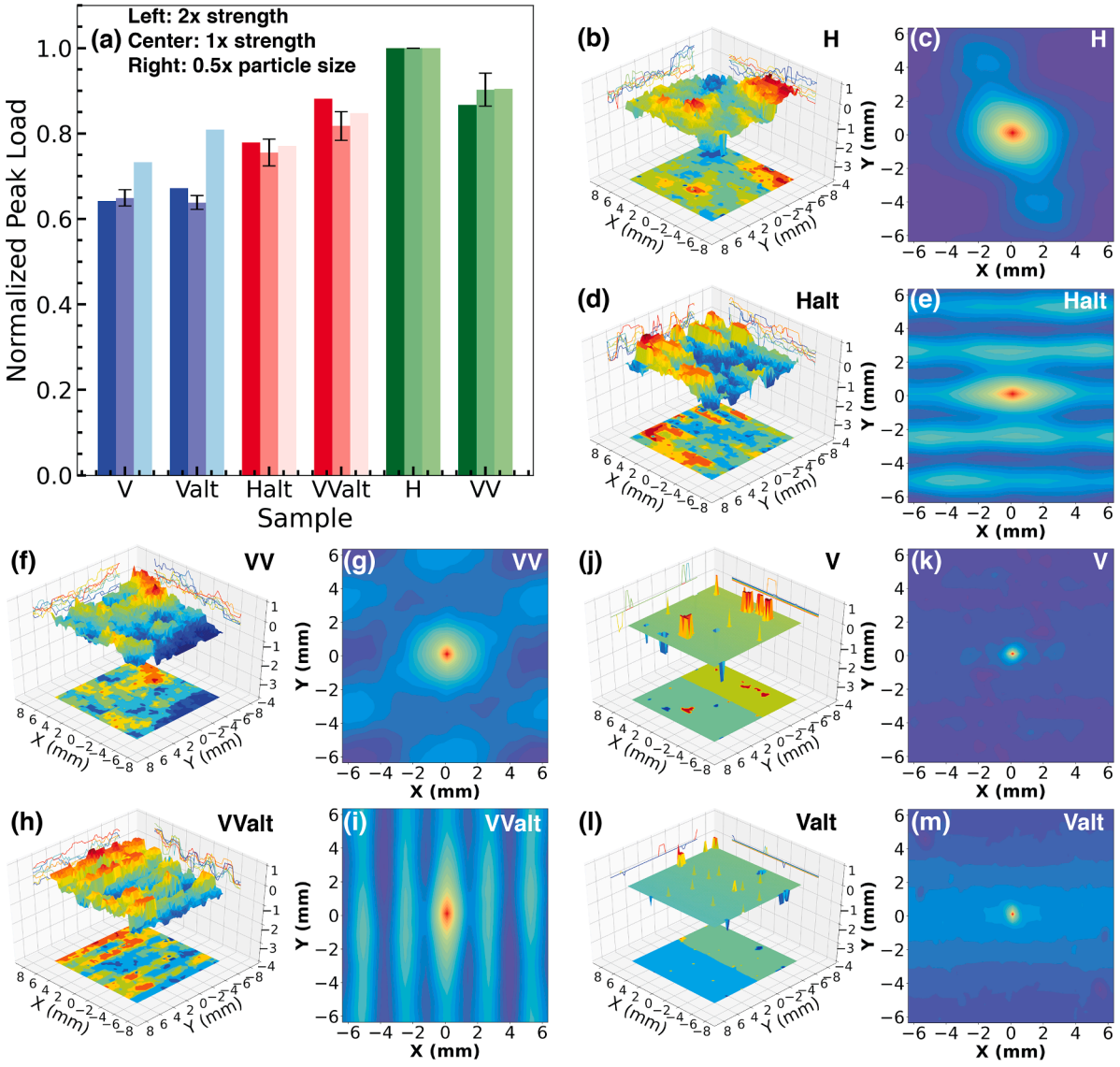

Fig. 12. (a) Normalized peak loads, with center columns as the base case, left columns (darker shade) are simulations with 2x the bonding strength and cohesion, right columns (lighter shade) are the simulations with 0.5x particle size. (b, d, f, j, h, l) show the fracture roughness profiles and (c),I,(g, k, i, m) the auto-correlation functions from simulations with 0.5x particle size (lighter shade in (a)).

Declaration of Competing Interest

The authors declare no conflict of interests.

Acknowledgment

The experimental work was supported by the U.S. Department of Energy, Office of Science, Office of Basic Energy Sciences, Geosciences Research Program under Award Number (DE-SC0001048). The computational work was supported by the U.S. Department of Energy, Office of Energy Efficiency and Renewable Energy (EERE), Office of Technology Development, Geothermal Technologies Office. Wang's contributions to writing of the manuscript were supported under the auspices of the U.S. Department of Energy by Lawrence Livermore National Laboratory under Contract DE-AC52-07NA27344. The 3D printed samples and Yoon's effort was supported by the Laboratory Directed Research and Development program (218328) at Sandia National Laboratories. Jiang's contributions to the writing of the manuscript were supported by Shuimu Tsinghua Scholar Program. Sandia National Laboratories is a multi-mission laboratory managed and operated by National Technology & Engineering Solutions of Sandia, LLC (NTESS), a wholly owned subsidiary of Honeywell International Inc., for the U.S. Department of Energy's National Nuclear Security Administration (DOE/NNSA) under contract DE-NA0003525. This written work is authored by an employee of NTESS. The employee, not NTESS, owns the right, title, and interest in and to the written work and is responsible for its contents. Any subjective views or opinions that might be expressed in the written work do not necessarily represent the views of the U.S. Government. The publisher acknowledges that the U.S. Government retains a non-exclusive, paid-up, irrevocable, world-wide license to publish or reproduce the published form of this written work or allow others to do so, for U.S. Government purposes. The DOE will provide public access to results of federally sponsored research in accordance with the DOE Public Access Plan.

References

[1] A.A. Griffith, VI. The phenomena of rupture and flow in solids, Philos. Trans. R. Soc. Lond. A 221 (582–593) (1921) 163–198, containing papers of a mathematical or physical character.

[2] C. Wang, L.J. Pyrak-Nolte, Fluid flow through fractures with corrugated surface roughness, ARMA Lett. 29 (2020) 17–22.
[3] S.R. Brown, Fluid flow through rock joints: the effect of surface roughness, J. Geophys. Res. Solid Earth 92 (B2) (1987) 1337–1347.
[4] P.S. Lang, A. Paluszny, R.W. Zimmerman, Hydraulic sealing due to pressure solution contact zone growth in siliciclastic rock fractures, J. Geophys. Res. Solid Earth 120 (6) (2015) 4080–4101.
[5] S. Luo, D. Kim, Y. Wu, Y. Li, D. Wang, J. Song, G. Zhang, Big data nanoindentation and analytics reveal the multi-staged, progressively-homogenized, depth-dependent upscaling of rocks' properties, Rock Mech. Rock Eng. 54 (2021) 1501–1532.
[6] K. Spokas, C.A. Peters, L. Pyrak-Nolte, Influence of rock mineralogy on reactive fracture evolution in carbonate-rich caprocks, Environ. Sci. Technol. 52 (17) (2018) 10144–10152.
[7] Y. Wu, Y. Li, S. Luo, M. Lu, N. Zhou, D. Wang, G. Zhang, Multiscale elastic anisotropy of a shale characterized by cross-scale big data nanoindentation, Int. J. Rock Mech. Min. Sci. 134 (2020), 104458.
[8] Yoon H., Ingraham M.D., Grigg J., Rosandick B., Mozley P., Rinehart A., ... & Dewers T. (2020). Impact of depositional and diagenetic heterogeneity on multiscale mechanical behavior of Mancos Shale, New Mexico and Utah, USA, in W. Camp, K. Milliken, K. Taylor, N. Fishman, P. Hackley, and J. Macquaker, eds., Mudstone Diagenesis: Research Perspectives for Shale Hydrocarbon Reservoirs, Seals, and Source Rocks: AAPG Memoir 120, p. 121–148. 10.1306/13672214M1213824.
[9] Y. Gao, Z. Liu, Q. Zeng, T. Wang, Z. Zhuang, K.C. Hwang, Theoretical and numerical prediction of crack path in the material with anisotropic fracture toughness, Eng. Fract. Mech. 180 (2017) 330–347.
[10] X. Zeng, Y. Wei, Crack deflection in brittle media with heterogeneous interfaces and its application in shale fracking, J. Mech. Phys. Solids 101 (2017) 235–249.
[11] N.D. Forbes Inskip, P.G. Meredith, M.R. Chandler, A Gudmundsson, Fracture properties of Nash point shale as a function of orientation to bedding, J. Geophys. Res. Solid Earth 123 (10) (2018) 8428–8444.
[12] F. Agliardi, S. Zanchetta, G.B. Crosta, Fabric controls on the brittle failure of folded gneiss and schist, Tectonophysics 637 (2014) 150–162.
[13] K. Benn, B. Allard, Preferred mineral orientations related to magmatic flow in ophiolite layered gabbros, J. Petrol. 30 (4) (1989) 925–946.
[14] I. Lonardelli, H.R. Wenk, Y. Ren, Preferred orientation and elastic anisotropy in shales, Geophysics 72 (2) (2007) D33–D40.
[15] L.J. Pyrak-Nolte, Fracture anisotropy: the role of fracture-stiffness gradients, Lead. Edge 26 (9) (2007) 1124–1127.
[16] H.R. Wenk, I. Lonardelli, H. Franz, K. Nihei, S. Nakagawa, Preferred orientation and elastic anisotropy of illite-rich shale, Geophysics 72 (2) (2007) E69–E75.
[17] S. Na, W. Sun, M.D. Ingraham, H. Yoon, Effects of spatial heterogeneity and material anisotropy on the fracture pattern and macroscopic effective toughness of Mancos Shale in Brazilian tests, J. Geophys. Res. Solid Earth 122 (8) (2017) 6202–6230.
[18] M.R. Chandler, P.G. Meredith, N. Brantut, B.R. Crawford, Fracture toughness anisotropy in shale, J. Geophys. Res. Solid Earth 121 (3) (2016) 1706–1729.
[19] L. Jiang, H. Yoon, A. Bobet, L.J. Pyrak-Nolte, Mineral fabric as a hidden variable in fracture formation in layered media, Sci. Rep. 10 (1) (2020) 2260.
[20] Liyang Jiang. Microstructural controls on macro-scale properties, Purdue University Graduate School. Thesis, 2022, https://doi.org/10.25394/PGS.19678824.v1.
[21] L. Jiang, H. Yoon, L.J. Pyrak-Nolte, A. Bobet, J. Morris, Calibration Data Set For Damage Mechanics Challenge on Brittle-Ductile Material, Purdue University Research Repository, 2021, https://doi.org/10.4231/QF39-Q924.
[22] P.A. Cundall, O.D. Strack, A discrete numerical model for granular assemblies, Geotechnique 29 (1) (1979) 47–65.
[23] D.O. Potyondy, P.A. Cundall, A bonded-particle model for rock, Int. J. Rock Mech. Min. Sci. 41 (8) (2004) 1329–1364.
[24] G. Venditti, V. Murali, A.A. Darhuber, Inkjet printing of surfactant solutions onto thin moving porous media, Colloids Surf. A 634 (2022), 127832.
[25] L.J. Pyrak-Nolte, D.D. Nolte, Approaching a universal scaling relationship between fracture stiffness and fluid flow, Nat. Commun. 7 (1) (2016) 10663.
[26] W. Jamróz, J. Szafraniec, M. Kurek, R. Jachowicz, 3D printing in pharmaceutical and medical applications–recent achievements and challenges, Pharm. Res. 35 (2018) 1–22.
[27] C.W.J. Lim, K.Q. Le, Q. Lu, C.H. Wong, An overview of 3-D printing in manufacturing, aerospace, and automotive industries, IEEE Potentials 35 (4) (2016) 18–22.
[28] N. Nachal, J.A. Moses, P. Karthik, C. Anandharamakrishnan, Applications of 3D printing in food processing, Food Eng. Rev. 11 (3) (2019) 123–141.
[29] R.J. Jackson, A. Wojcik, M. Miodownik, 3D printing of asphalt and its effect on mechanical properties, Mater. Des. 160 (2018) 468–474.
[30] N. Leach, 3D printing in space, Arch. Des. 84 (6) (2014) 108–113.
[31] Y.W.D. Tay, B. Panda, S.C. Paul, N.A. Noor Mohamed, M.J. Tan, K.F. Leong, 3D printing trends in building and construction industry: a review, Virtual Phys. Prototyp. 12 (3) (2017) 261–276.
[32] J.Y. Wong, A.C. Pfahnl, 3D printed surgical instruments evaluated by a simulated crew of a Mars mission, Aerosp. Med. Hum. Perform 87 (9) (2016) 806–810.
[33] J. Xu, L. Ding, P.E. Love, Digital reproduction of historical building ornamental components: from 3D scanning to 3D printing, Autom. Constr. 76 (2017) 85–96.
[34] J. Zhang, J. Wang, S. Dong, X. Yu, B. Han, A review of the current progress and application of 3D printed concrete, Compos. Part A 125 (2019), 105533.